The occurrence of staircases in ITG turbulence with kinetic electrons and the zonal flow drive through self-interaction (EP)

(iD) A. Weikl, A. G. Peeters, F. Rath, et al.

COLLECTIONS

(EP) This paper was selected as an Editor's Pick

View Online   Export Citation   CrossMark

ARTICLES YOU MAY BE INTERESTED IN

Comparisons and physics basis of tokamak transport models and turbulence simulations
Physics of Plasmas **7**, 969 (2000); https://doi.org/10.1063/1.873896

Electron temperature gradient driven turbulence
Physics of Plasmas **7**, 1904 (2000); https://doi.org/10.1063/1.874014

Analysis of zonal flow pattern formation and the modification of staircase states by electron dynamics in gyrokinetic near marginal turbulence
Physics of Plasmas **28**, 072305 (2021); https://doi.org/10.1063/5.0054358

The occurrence of staircases in ITG turbulence with kinetic electrons and the zonal flow drive through self-interaction

A. Weikl, A. G. Peeters, F. Rath, F. Seiferling, R. Buchholz, S. R. Grosshauser, and D. Strintzi
Physics Department, University of Bayreuth, Universitätsstrasse 30, Bayreuth 95440, Germany

Large scale structures in the $E \times B$ shearing rate, known as staircases, are shown to form in nonlinear gyro-kinetic turbulence simulations with kinetic electrons. However, in many cases, a small scale structure in the shearing rate is observed that appears to prevent the formation of staircases. The small scale structures are interpreted to be linked to the self-interaction of turbulent modes connected with the double periodic boundary conditions on the torus. The self-interaction is a newly discovered mechanism for zonal flow generation and is shown to scale proportional to the normalized Larmor radius. The mechanism is also affected by magnetic shear, being weaker at larger values. *Published by AIP Publishing.* https://doi.org/10.1063/1.5035184

I. INTRODUCTION

Recent work[1,2] has revealed that zonal flows in global ITG turbulence with adiabatic electrons self-organize in the so-called staircase structures. These structures have subsequently been observed in a gradient as well as flux driven flux tube simulations and have been shown to affect the dynamics close to the nonlinear threshold of ITG turbulence.[3,4] Furthermore, collisions at levels relevant to the experiment do not prevent staircase formation.[5,6] However, to our knowledge, the existence of staircases has not been verified in turbulence simulations with kinetic electrons. Indeed, their existence in this case is non-trivial, since zonal flows are then generally found to be weaker compared with the adiabatic electron case. Consequently, it is unclear if staircases form under these more experimentally relevant conditions. In this paper, it will be shown that staircases are also obtained with kinetic electrons, but not for all cases. In studying the staircase formation with kinetic electrons, a new mechanism for zonal flow drive is revealed: the self-interaction of a turbulent mode due to the double periodicity of a toroidal flux surface. The self-interaction is connected with the parallel boundary conditions and is not necessarily physical when obtained in a flux tube simulation with a small normalized Larmor radius. It will be shown that, when it does occur, it can have a profound effect on staircase formation and the heat flux behaviour close to the threshold. Furthermore, it will be argued that the self-interaction can indeed occur under some conditions.

This paper is structured as follows: In Sec. II, the self-interaction mechanism is discussed in detail. In Sec. III, an initial numerical investigation of the heat conduction as a function of the temperature gradient length is presented. Small scale structures in the $E \times B$ shearing rate are observed and their physical nature is discussed in Sec. IV, where they are linked to the self-interaction. Section V then investigates the parameter dependence of the self-interaction and Sec. VI exploits the gained knowledge to confirm the existence of staircases with kinetic electrons. A synopsis and concluding remarks are given in Sec. VII.

II. ZONAL FLOW DRIVE THROUGH SELF-INTERACTION

In a tokamak, when following the field lines, the modes are twisted due to the magnetic shear. The ballooning transform,[7] to which the flux tube description is closely related, incorporates this effect through the dependence of the radial wave vector on the poloidal angle. In the flux tube formulation,[8] the same effect is present, albeit often hidden in the metric of the field aligned coordinates. For the ballooning transform, the field line is extended to infinity, and the radial wave vector keeps increasing after one turn. In the flux tube formulation (employed in this study), the computational domain contains only one turn of the field line, with the parallel boundary conditions at the end point of the field line connecting the mode to a mode with a higher radial wave vector. This boundary condition is in essence equivalent to the increasing radial wave vector of the ballooning transform.

GKW,[9] the code employed for the flux-tube simulations of this investigation, uses straight field line Hamada coordinates[10,11] (ψ, ζ, s). Here, ψ represents the flux label, ζ is the binormal coordinate, and s is the coordinate parallel to the field, where ζ and s are normalized to obtain a computational domain $\zeta \in [0, 1]$ and $s \in [-1/2, 1/2]$, respectively. The high field side position is given by $s = \pm 1/2$. The double periodic boundary conditions for the phase-space distribution function (f) on the toroidal flux surface then are

$$
\begin{aligned}
f(\psi, \zeta, s) &= f(\psi, \zeta + 1, s) \\
f(\psi, \zeta, s) &= f(\psi, \zeta - q, s + 1),
\end{aligned}
\tag{1}
$$

where the first represents the periodicity in the toroidal and the second in the poloidal direction. The latter boundary condition takes into account that, when moving over one turn along the field ($s = +1$), the binormal coordinate undergoes a change $+q$, where q is the safety factor.

The distribution function in the radial (ψ) and binormal (ζ) directions is represented by Fourier modes

$$f = \sum_{\mathbf{k}} \hat{f}(k_\psi, k_\zeta, s) \exp\left[ik_\psi\psi + ik_\zeta\zeta\right] + c.c., \quad (2)$$

while the direction along the field line (s) is treated in real space. A proper choice of the binormal wave vectors (k_ζ) leads to a periodic solution on the domain $\zeta \in [0, 1]$ and the first condition of Eq. (1) is automatically satisfied. To fulfill the second condition, the safety factor is chosen such that $q(0)k_\zeta = 2k\pi$, with $k = 1, 2, \ldots$ in the centre ($\psi = 0$) of the radial domain. Then, the modes are resonant in the centre of the domain. This choice can be motivated by the high toroidal mode numbers of the ITG turbulence, leading to a resonant surface in close proximity to the local surface considered in the computation. Although the modes are resonant in the centre of the box, the magnetic shear $\hat{s}$ must be considered. The change in the safety factor taken as

$$q(\psi) = q(0) + \left.\frac{\partial q(\psi)}{\partial \psi}\right|_{\psi=0} \psi \quad (3)$$

leads to non-resonant modes away from the centre. Using this expression for the safety factor, it is possible to satisfy the second condition of Eq. (1) by imposing

$$\hat{f}\left(k_\psi, k_\zeta, \frac{1}{2}\right) = \hat{f}\left(k_\psi + k_\zeta\frac{\partial q}{\partial \psi}, k_\zeta, -\frac{1}{2}\right) \quad (4)$$

as the boundary condition in the s-direction. This means that, at the end points of a field line, modes with a different radial wave vector (k_ψ) couple. The shift in the radial wave vector is

$$\Delta k_\psi = k_\zeta\frac{\partial q}{\partial \psi} = k_\zeta\hat{s}\frac{q}{\epsilon}, \quad (5)$$

where $\epsilon = r/R$ is the inverse aspect ratio. However, commonly the poloidal wave vector (k_θ) is used. The relation to the binormal wave vector depends on the employed geometry. For the circular concentric flux surfaces used in this work, the shift in terms of k_θ becomes

$$\Delta k_\psi = k_\theta 2\pi\hat{s}\frac{q}{\epsilon}\frac{1 + \epsilon}{(1 + (q/\epsilon)^2(1 - \epsilon^2))^{\frac{1}{2}}}. \quad (6)$$

This shift is used to set up the k_ψ grid. In order to allow for equal resolution in radial and binormal directions, an integer $i_k \approx 2\pi\hat{s}$ is introduced, so that the step size of the radial wave vector is $\delta k_\psi = \Delta k_\psi/i_k$. The boundary conditions as formulated above are globally consistent.[12,13]

From the discussion on the boundary conditions, the zonal flow drive through self-interaction can be understood easily. Consider an unstable ITG mode with a wave vector (k_ψ, k_ζ). Over the parallel boundary conditions, this mode will connect with the $(k_\psi \pm \Delta k_\psi, k_\zeta)$ mode, i.e., parallel streaming can transfer energy to higher or lower k_ψ modes. If a nonlinear interaction between the (k_ψ, k_ζ) and $(k_\psi \pm \Delta k_\psi, k_\zeta)$ modes can occur, it will transfer energy into the $(2k_\psi \pm \Delta k_\psi, 2k_\zeta)$ as well as the $(\pm\Delta k_\psi, 0)$ mode. The latter is a zonal mode and, as the shear-periodic boundary condition connects modes with a distinct difference in the radial wave vector, a zonal mode with

the distinct radial wave vector Δk_ψ is driven. The self-interaction can therefore directly drive specific zonal modes. Several points should be noted. The self-interaction mechanism uses all radial modes with the same k_ζ to drive the same distinct zonal mode. The $(2k_\psi \pm \Delta k_\psi, 2k_\zeta)$ mode is driven generally only by one pair of modes.

The proposed self-interaction mechanism shares similarities with the familiar modulation instability.[14,15] Both can be explained with a quadratic nonlinearity leading to wave interaction which drives the zonal mode. However, the physical mechanism of the self-interaction differs from the one of the modulation instability. There, the side bands grow exponentially due to the interaction of the zonal flow with the pump wave, leading to an exponential growth of the zonal flow, which is a smooth function of the radial wave vector. In the self-interaction mechanism, the side bands obtain their energy through the flow along the field lines and the mechanism drives zonal modes at distinct radial wave vectors. As such, a mode is driven by all turbulent modes with the same k_ζ; an effective invocation of feedback on the driving modes is not possible, so an algebraic rather than an exponential growth is observed, which is shown later on. Following from that, a 3D description is a mandatory requirement to obtain the self-interaction. It should also be mentioned that an interaction between the two modes must not necessarily occur in a turbulent plasma. Following a field line over one poloidal turn, it is in general shifted in the toroidal direction. At a fixed toroidal angle, the $(0, k_\zeta)$ and $(\pm\Delta k_\psi, k_\zeta)$ mode might be uncorrelated, thus yielding a zero time averaged drive.

As stated above, the boundary conditions applied in a flux tube are consistent with the double periodicity of the toroidal flux surface and a flux tube can describe the dynamics inside the flux surface without approximation. Nevertheless, an additional approximation is usually made in the case of a small normalized Larmor radius. In this case, the description of the turbulence on the whole flux surface would require a large amount of k_ζ modes. In order to save computational resources, it is assumed that the turbulence on a smaller wedge of the surface is equivalent to all other parts. Then, the computational domain is represented by a part of the toroidal circumference and the first boundary condition of Eq. (1) is assumed to apply on this smaller domain (renormalizing ζ such that the domain is still $[0, 1]$). It must be stressed that this condition is of a different nature compared with the exact double periodic boundary condition described above. The boundary condition on the smaller domain can only be justified using a statistical argument, i.e., on average the turbulence on all the wedges is similar. Such an argument fails if the description of the physics processes demands that no correlation between the turbulence in the different wedges occurs.[16] The self-interaction is an effect that can be overestimated if the statistical argument is applied: If a small wedge is considered, following the field line for one poloidal turn will in general lead to a toroidal shift outside the domain of the wedge. The applied periodic boundary conditions on the ζ domain map the perturbation back into the computational domain, possibly generating a spatially localized correlation between modes that do not exist on the full flux surface.

As a consequence, the self-interaction can only be properly calculated if the whole flux surface is considered. Of course, every flux tube simulation can be considered to describe a whole flux surface provided the normalized Larmor radius is large enough. However, experimentally relevant normalized Larmor radii require a large amount of binormal modes. Assuming that the turbulence requires the resolution of wave lengths up to $k_\theta \rho \approx 1$, with $k_\theta \approx nq/r$ where n is the toroidal mode number, ρ is the Larmor radius, and r is the radius of the poloidal flux surface, then a full surface simulation requires

$$N_\theta = \frac{r}{qR\rho_*} \qquad (7)$$

k_θ modes. In the equation above, $\rho_* = \rho/R$, with R being the major radius. So, for current day experiments $N_\theta \geq 64$ is commonly assumed.

Furthermore, following the argument above, it might appear that the self-interaction has to be considered unphysical; as commonly, in adiabatic simulations, no correlation of the turbulent modes over long distances in the flux surface is found. However, if kinetic electrons are considered, turbulence does exhibit a correlation over long distances. To show this, the normalized correlation function C_N is evaluated for an adiabatic and a kinetic standard simulation (see Sec. III for details on the numerical setup). C_N is determined using only the turbulent part (without the zonal mode) of the perturbed electrostatic potential, the values are averaged over a stationary turbulent period.

Figure 1 shows the resulting correlation function in the binormal direction, summed over all radial modes. Here it is evident that, if kinetic electrons are considered, C_N does not go to (almost) zero, as in the adiabatic simulation. Instead, a finite value for long distances can be assumed. To back up this claim, the local maxima are fitted with a function of the form $a + \exp(-b\theta)$ where a long range correlation of $a = 0.052$ is found. This is attributed to the increased electron velocity. Similar results are also found for other simulations with different parameters or resolutions.

In this section, the self-interaction mechanism has been discussed in some detail, as it will enter in the simulations discussed in Sec. II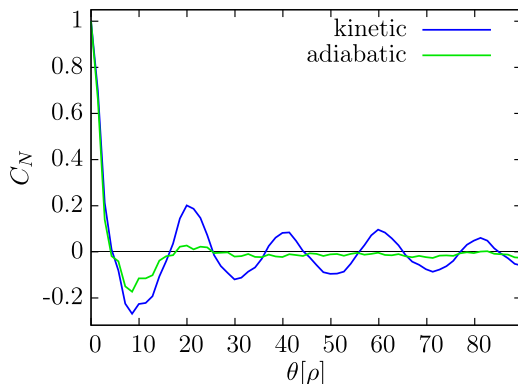I. The reason why it appears in simulations with kinetic electrons, but has not been observed in the simulations using adiabatic electrons, is the long extension of the mode structure along the field line in the kinetic electron case.[17,18] This leads to an increased connection via the boundary conditions in the s-direction.

III. HEAT FLUX NEAR MARGINAL STABILITY

In this section, a numerical investigation of the heat transport close to the nonlinear threshold of ITG turbulence with kinetic electrons is presented. The flux-tube version of the nonlinear Eulerian gyro-kinetic code GKW[9] is used in this study. The simulations are gradient driven, neglect plasma rotation as well as collisions, and have a standard parameter set compliant to the well known cyclone base case: safety factor $q = 1.4$, magnetic shear $\hat{s} = 0.78$, inverse aspect ratio $\varepsilon = 0.19$, and density gradient $R/L_n = 2.2$. Electrons are treated kinetically with an electron to ion-mass-ratio $m_e/m_i = 2.72 \times 10^{-4}$ (deuterium). The temperature gradient (R/L_T) is varied to investigate the heat flux close to the threshold value and is in general smaller than the cyclone base case value due to the stronger instability connected with the kinetic electrons. Finally, electron and ion temperatures (T) as well as their gradients are chosen to have the same value, the standard value being $R/L_T = 3.5$. To reduce the computational cost, a small electron plasma beta $\beta_e = 3 \times 10^{-4}$ is assumed and the simulations retain the shear Alfvén wave physics. With this choice, the shear Alfvén wave propagates at a velocity comparable to the electron thermal speed, thus allowing an optimal time step. The impact of the electro-magnetic effects has been checked for a standard simulation and no significant differences in the heat flux or zonal flow dynamics compared with the pure electro-static case are found.

To be compliant to the commonly used depictions, numerically obtained spectra are presented as a function of the poloidal rather than the binormal wave vector. The used grid sizes are shown in Table I. Here, N_ψ (N_θ) is the number of radial (binormal/poloidal) modes, N_s is the number of points along the magnetic field, N_μ is the number of points in the magnetic moment, and $N_{v_\parallel}$ is the number of points in the parallel velocity direction. The maximal radial and poloidal wave vectors are denoted by $k_{\psi,\text{max}}$ and $k_{\theta,\text{max}}$. G1 is a grid with a reduced resolution and is assumed to exhibit some inadequacies. It is used in Secs. V and VI as an additional comparison. G2 is the standard resolution used in most of the simulations and G3 a high resolution case that is computationally demanding. G2-b is a variation used for individual tests. To counteract the increased computational cost, the parallel resolution in the G3 case is reduced. To ensure that

FIG. 1. Correlation function C_N in the binormal/poloidal direction summed over all radial modes for simulations with standard parameters and a grid G3 (see Sec. III).

TABLE I. Overview of used grid sizes.

	N_ψ	N_θ	N_s	N_μ	$N_{v_\parallel}$	$k_{\psi,\text{max}}$	$k_{\theta,\text{max}}$
G1	43	11	32	9	64	3.5	1.4
G2	83	21	32	9	64	3.4	1.4
G2-b	165	21	32	9	64	3.4	1.4
G3	165	41	16	9	64	3.4	1.4

this reduction does not affect the results quantitatively in a noticeable manner, the so-called Rosenbluth-Hinton test[19] is employed. Here, the evolution of the zonal potential is investigated and compared (similar to Ref. 5). This also guarantees that no over-damping occurs. All the wave vectors are given in relation to the Larmor radius $\rho = m_d v_{th}/eB$ with m_d the deuterium mass, e the elementary charge, B the magnetic induction, and $v_{th} = \sqrt{2T/m_d}$ is the thermal velocity. Note that a factor two is used in the latter definition, and the thermal velocity is $\sqrt{2}$ larger compared with the often employed sound speed. The size of the radial wave vector grid is determined by the condition of Eq. (6), where normally $i_k = 5$ is used to ensure a comparable resolution in the radial and binormal directions. For the zonal mode, the sixth order scheme along the magnetic field is used, and the dissipation coefficients are $D_x = 0.1$, $D_y = 0.1$, $D_s = 1$, and $D_{v_\parallel} = 0.2$ (see Ref. 4 for details on the implementation of the scheme and dissipation).

Figure 2 shows the normalized ion heat conduction coefficient (χ, normalized to $\rho^2 v_{th}/R$) as a function of the ion temperature gradient length (R/L_T). It is obtained from the time average over a sufficiently long stationary period. The curve with resolution G1 shows an appreciable difference from the G2 and G3 resolution cases, and it can be concluded that the resolution is insufficient to obtain accurate results. The G2 and G3 cases, however, are in good agreement, showing that the result is converged in these cases. In contrast to the simulations with adiabatic electrons,[3–5] the heat flux goes smoothly to zero, and there is no sign of a finite heat flux threshold. Note that χ does not go linearly (estimated for $\chi \gtrsim 1$) in R/L_T to zero, instead a flattening for small χ is seen. Here, a small but finite heat conduction coefficient is found. In these cases, a late onset of a suppressed turbulent state is not anticipated, as considerably long simulations $>7000R/v_{th}$ do not exhibit signs of suppressed turbulence. The appearance of the finite heat flux threshold in the adiabatic electron case, in which a jump in the heat flux is observed at the threshold, is connected with a staircase structure in the $E \times B$ shearing rate.[4] Just below the threshold, the staircase is fully developed and turbulence suppression
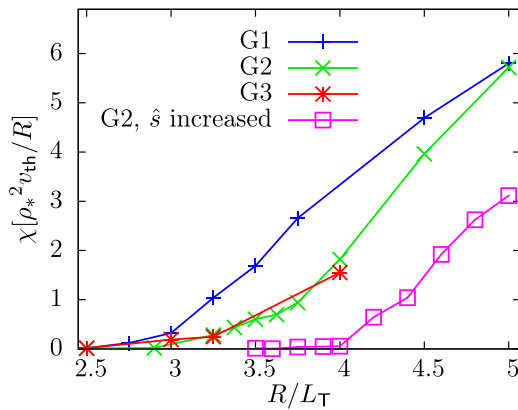
occurs over the whole radial domain. At the threshold, the radial profile of the structure changes with one of the crossings of the $E \times B$ shearing rate through zero becoming less steep. At the latter location, avalanches form, which then carry the heat through the regions of high $E \times B$ shear. The smooth functional dependence of the heat conduction coefficient on the gradient length in the case of kinetic electrons suggests that staircases do not form in these cases.

To investigate this, the radial profile of the $E \times B$ shear rate $\omega_{E \times B} = \partial^2 \phi / \partial \psi^2 / 2B$ for the standard parameter set with $R/L_T = 3.5$ is shown in Fig. 3. Here, $\omega_{E \times B}$ is normalized with v_{th}/R, the potential is normalized with $e/(\rho_* T)$, and ψ is normalized with ρ_* and B with the field on the magnetic axis. It can be observed that small scale fluctuations, that appear in quasi-periodic bunches, dominate the $E \times B$ shearing profile. These small scale structures are remarkably stationary in time, as is evident from the relatively large time interval over which the signals presented in Fig. 3 have been averaged. The amplitude of the small scale $E \times B$ shearing rate structures is considerably larger than the ITG growth rate ($\gamma = 1.5 \times 10^{-1} v_{th}/R$), indicated by the horizontal lines. These structures, therefore, do not stabilize the ITG as efficiently as the Waltz rule $\omega_{E \times B} \approx \gamma$ would predict,[20] presumably due to their very short wavelength. In fact, it is at present unclear if any appreciable ITG stabilization is generated. It should be noted that the fine scale structure is relatively stationary and the reduced impact of shear stabilization cannot be explained through a temporal dependence as in Ref. 21.

The behaviour described above is observed in all simulations that use standard parameters. A typical staircase

FIG. 2. Heat conductivity χ averaged over a stationary period as a function of the temperature gradient length R/L_T. The results of simulations with the three different grid sizes (see Table I) are shown. Furthermore, the results from simulations with an increased magnetic shear $\hat{s}$ and resolution G2 are shown, further discussed in Sec. VI.
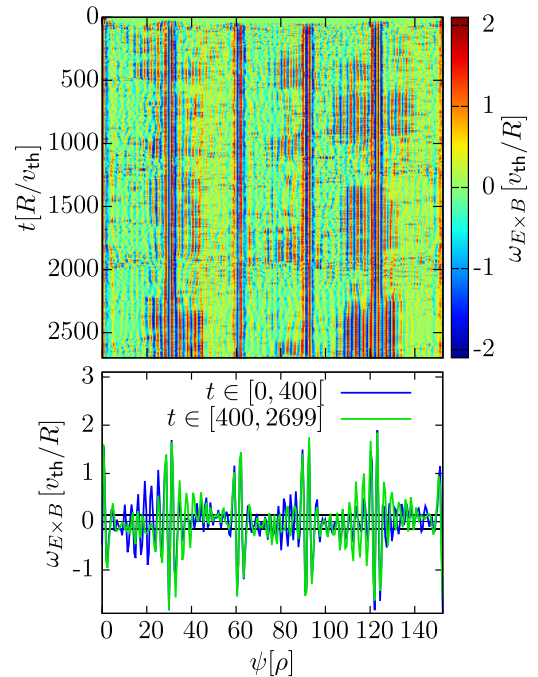

FIG. 3. Top: Evolution of the radial $E \times B$ shearing profile $\omega_{E \times B}$ for a simulation with the standard parameter set and grid size G3 (colour online). Bottom: Averaged profiles in the initial and the stationary states, respectively. The expected linear ITG growth rate of $\gamma = 1.5 \cdot 10^{-1} v_{th}/R$ is indicated with black horizontal lines. Note that periodic boundary conditions apply in the radial direction.

structure cannot be made out in the radial shear profiles, even when attempting to filter out the small scale fluctuations. Although avalanches in the heat flux are observed (but not shown), these do not have starting or ending points at fixed radial positions, as is observed for the staircase structures obtained with adiabatic electrons.[2–5] In conclusion, the dependence of the heat conduction on the gradient, the profile of the $E \times B$ shear, and the radial distribution of avalanches all indicate that staircases do not form in these cases.

IV. PHYSICAL NATURE OF THE SMALL SCALE $\omega_{E \times B}$ STRUCTURES

The small scale structures in the $E \times B$ shearing rate are caused by the self-interaction connected with the parallel boundary conditions, which will be shown below. For that task, the results of a simulation with grid resolution G3 and the aforementioned standard parameters (with $R/L_T = 3.5$) are discussed. After an initial linear phase, the simulations exhibit a quasi-stationary, turbulent state in which the self-interaction drives the distinct zonal modes. Figure 4 shows the electric potential $|\phi|$, taken as a measurement of the mode intensity, in the k_ψ–k_θ-plane (only positive wave vectors are shown).

Here, several observations can be made. The ITG turbulence generates a maximum potential amplitude located at low k_ψ and $k_\theta \rho \approx 0.35$. The extended ITG mode structure along the magnetic field line, connected with the fast passing electrons, leads to the generation of a contribution at higher k_ψ. The visible enhancement at higher k_ψ due to the parallel boundary conditions is evident from the marks (white circles in the online version) indicating Δk_ψ given by Eq. (6) as a function of k_θ. The nonlinear interaction between modes grouped around $k_\psi \approx 0$ and those at $k_\psi = \Delta k_\psi$ then drives the zonal mode, which can be seen as a discontinuous band at the bottom of the figure. Here, a correlation between the ITG-maximum and an exceptional strong drive of the zonal modes can be discerned.
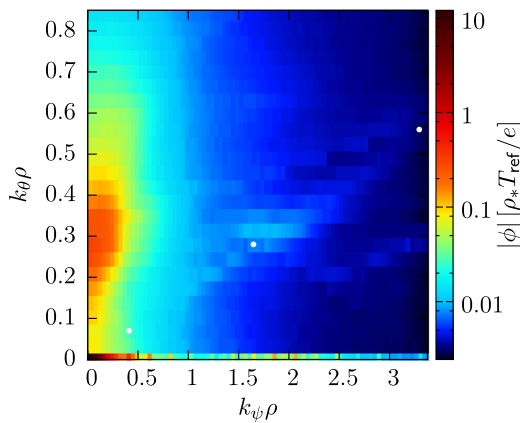
The radial spectrum of the absolute value of the electrostatic potential $|\phi|$ at $k_\theta = 0$ is shown in Fig. 5 (mind the logarithmic scaling of k_ψ here). As discussed in Sec. II, the self-interaction mechanism drives zonal flows with a distinct radial wave vector. Indeed, the spectrum in Fig. 5 shows spikes at distinct positions. Furthermore, these spikes coincide with the radial shift Δk_ψ due to the boundary conditions which are marked by the vertical lines (red in the online version), indicating the modes driven through self-interaction. Moreover, if the relative size of the spikes is taken into account, the relation to the ITG-maximum is nicely visible. In Fig. 5, the radial spectrum of the $E \times B$ shear rate is also depicted. It can be seen that the spikes at high k_ψ dominate the $\omega_{E \times B}$ spectrum. This is consistent to the form of the radial shear profile presented in Fig. 3. The wave length of the small scale $\omega_{E \times B}$ structures shown there is consistent with the shift Δk_ψ and is a direct consequence of the self-interaction mechanism.

Furthermore, the question arises whether the intensity of the driving modes is in accordance with the growth of the spikes. Therefore, the required growth time t_G for the individual spikes is coarsely estimated by mimicking the mechanism of the self-interaction. Motivated by an analysis of the momentum balance between the Reynolds stress and the zonal flow vorticity, t_G for a zonal mode ϕ_{ZF} driven by the modes at k_θ is given as

$$t_G = \frac{|\phi_{ZF}(\Delta k_\psi, 0, s)|}{\sum_{k_\psi} k_\psi k_\theta |\phi(k_\psi, k_\theta, s)| |\phi(k_\psi + \Delta k_\psi, k_\theta, s)|}. \quad (8)$$

Here, ϕ_{ZF} is taken as the size of the spikes $\Delta|\phi|$ which are taken as the difference between the potential at the position of the spike and a logarithmic baseline. Generally, the two nearest points in each direction are taken to define the baseline. In a few cases, where this is not possible, only the adjacent points are used. It should be noted that due to turbulent fluctuations, this method becomes less exact for spikes being

FIG. 4. Spectral slice in k_ψ- and k_θ-directions of the electrostatic potential $|\phi|$, averaged over the stationary turbulent state. The simulation uses the standard parameter set and grid resolution G3. The radial shift given in Eq. (6) corresponding to each k_θ is indicated by the white (in the online version) circles. Take notice of the discontinuous behaviour of the zonal mode at the bottom of the figure and that only a portion of the spectral plane is shown.
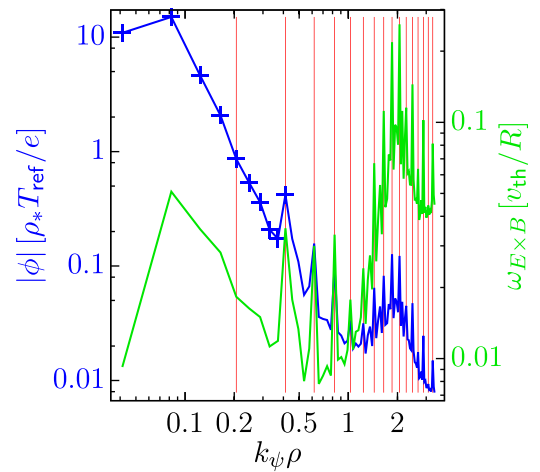

FIG. 5. Radial spectrum at $k_\theta = 0$ of $|\phi|$ (corresponding to the left axis, blue in the online version) and $\omega_{E \times B}$ (corresponding to the right axis, green in the online version). It is averaged over the stationary state of a simulation with the standard parameter set and the grid G3. Δk_ψ is indicated with vertical lines (red in the online version). Note the logarithmic scaling of k_ψ in comparison with Fig. 4.

small in relation to the baseline, which can be anticipated, for example, in Fig. 5. These results are compared to the observed growth rates in simulations with standard parameters and resolution G2. For this, the spikes are first suppressed, i.e., the modes determined via Eq. (6) are set to a vanishing value. Then, the suppression is lifted and the mode grows to a stationary state. Results of this process are presented in Fig. 6. Here, the evolution of the individually normalized electrostatic potential $|\phi|/|\phi|_{\max}$ for some of the zonal modes that are resonant to the self-interaction after the suppression is depicted exemplarily. The end of the suppression occurs at $t = 900\,R/v_{\mathrm{th}}$ and to indicate the later stationary state its average value is depicted as a horizontal line. The time needed for the mode to grow to the stationary state is found to be around $100\,R/v_{\mathrm{th}}$ to $150\,R/v_{\mathrm{th}}$, which is well above the predicted growth time estimated with Eq. (8), being $10\,R/v_{\mathrm{th}}$ to $50\,R/v_{\mathrm{th}}$. So it is concluded that the self-interaction mechanism is able to drive the observed spikes in the zonal mode. In Fig. 6, it can also be seen that the self-interaction leads to an algebraic growth and not to an exponential growth, which one would expect from the modulation instability.

V. PARAMETER DEPENDENCE OF THE SELF-INTERACTION

The above result on small scale structures in the $E \times B$ shearing rate raises several questions: Do they prevent the formation of a staircase structure, or is it merely an additional artefact? Is the self-interaction relevant for any experiment or future reactor? And if it is not relevant, do flux tube calculations produce inaccurate results because of these structures? To answer these questions, the parameter dependence of the self-interaction is studied below.

In the discussion in Sec. II, it was argued that every flux tube simulation can be thought of as correctly describing a whole flux surface, provided the normalized Larmor radius is chosen consistent with the computational domain. For the resolutions used in this paper, these normalized Larmor radii are G1: $\rho_* = \rho/R = 1.9 \times 10^{-2}$, G2: $\rho_* = 9.5 \times 10^{-3}$, and G3: $\rho_* = 4.75 \times 10^{-3}$. Consequently, if one assumes to

describe the entire flux surface, it cannot be assumed that the resolutions of the smaller grids represent current experiments, only the case G3 can be deemed relevant. From the discussion in Sec. II it is clear that one can expect the self-interaction to decrease with increasing device size, i.e., decreasing normalized Larmor radius. For the flux tube simulations, the change in the normalized Larmor radius implies a large amount of modes. The scaling of the self-interaction with the number of modes can also be argued as follows: The potential perturbations are unaffected when the resolution in real space is doubled for a fixed box size. Parseval's theorem then states that that the turbulence intensity calculated by summing the Fourier amplitudes of all modes $I \propto \sum_{\mathbf{k}} |\hat{\phi}|^2$ should be unaffected. If the resolution is doubled in the binormal direction, the higher mode density in $\mathbf{k}$−space then implies that each of the modes carries an intensity that is two times smaller. Since the self-interaction is connected to the nonlinearity, it scales proportional to the intensity, and the drive of each of the spikes can be assumed to be two times smaller. Since the number of k_θ modes that must be kept in the simulation of a full flux surface scales as $1/\rho_*$, it is expected that the intensity of the spikes is roughly proportional to the normalized Larmor radius. Note that the same argument does not directly apply to the doubling of resolution in the radial direction. Although doubling the resolution in this direction leads to a similar decrease in the turbulence intensity, all modes with the same k_θ drive the same zonal flow mode with $k_\psi = \Delta k_\psi$ and, consequently, the same amplitude in this mode can be expected.

The above-mentioned scaling with the number of modes is shown in Fig. 7 where the resulting spike intensities $\Delta|\phi|$

FIG. 7. Intensities of the spikes in the zonal mode caused by self-interaction. The simulations are using the standard parameter set; the four different grid sizes shown in Table I are used. Furthermore, the results of a simulation with an increased m_e/m_i and the grid G2 are shown. Negative values are omitted and the neighbouring points are not connected.
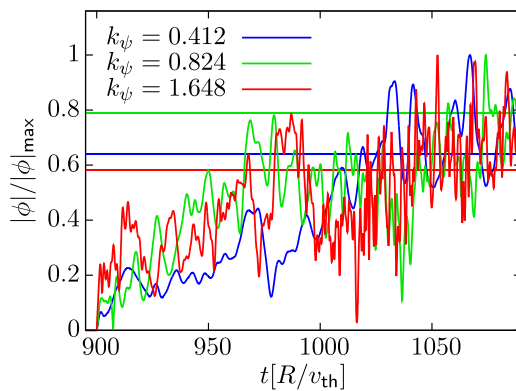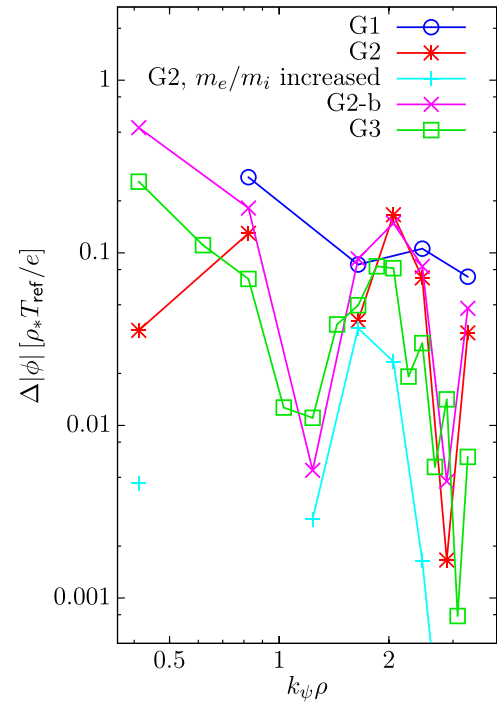
FIG. 6. Evolution of the individually normalized electrostatic potential $|\phi|/|\phi|_{\max}$ after an initial suppression for some of the zonal modes that are resonant to the self-interaction. The end of the suppression occurs at $t = 900\,R/v_{\mathrm{th}}$. As a comparison, the corresponding average over the later stationary state is depicted as a horizontal line.

(see Sec. IV for calculation) are depicted for the different resolutions (see Table I) used in this paper. For the grids G2 and G3, beginning from small k_ψ, the spike size decreases, after a minimum at $k_\psi \rho \approx 2$, another maximum appears, and then the $\Delta|\phi|$ decreases again. The grid G1 has an insufficient k_ψ-resolution to show this behaviour. The behaviour of the grids G2 and G3 is in accordance with the binormal spectrum of ϕ, summed in the radial direction. As already mentioned, the calculation of the spikes is tainted by turbulent fluctuations. This leads to small discrepancies and is taken as an explanation for the (albeit very small) negative spike sizes found. Concluding from that, high spikes located in regions with a low turbulent baseline (region at $k_\psi \rho \approx 2$) are deemed the most expressive in this analysis. If the results of the different grid sizes are compared, the expected decrease in the spike intensities with increasing resolution is observed. Comparing $\Delta|\phi|$ for corresponding k_ψ, the relation between the grids G1 and G2 does exhibit an averaged relation of $\Delta|\phi|_{G1}/\Delta|\phi|_{G2} \approx 2$, which is found quite consistently over the whole k_ψ range. For the grids G2 and G3, again an averaged relation of $\Delta|\phi|_{G2}/\Delta|\phi|_{G3} \approx 2$ is found; however, deviations from that value for many points are found. These are attributed to turbulent fluctuations. The reduction in the spike size for increasing resolutions suggests that at small ρ_* no significant self-interaction can occur. Still, at the resolution G3, which corresponds to a normalized Larmor radius of $\rho_* = 4.75 \times 10^{-3}$, the effect is remarkably strong as seen in Secs. III and IV, and a significantly large mode density (smaller ρ_*) would be required to eliminate the small scale structures in the $\omega_{E \times B}$ shearing rate. To test the aforementioned argument of the scaling, a simulation with standard parameters and resolution G2-b is used, and the results are shown in Fig. 7. Here, compared to G2, the number of radial modes is doubled and the number of binormal modes is kept the same. Consequently, the strength of the spikes observed here is expected to be similar to the G2 case. If both results are compared, a sub-par agreement for spikes at lower k_ψ is found. It is assumed to be caused by the different resolutions in the radial and binormal direction having a higher influence on spikes that are small in relation to the baseline. The results at higher k_ψ do compare relatively well and are taken to be more credible as the relative spike size is higher (compare, for example, in Fig. 5). Thus, the argument is assumed to hold in the framework of this analysis.

Furthermore, the influence of the electron-ion-mass-ratio of m_e/m_i is investigated. The self-interaction is caused by the long extension of the mode along the field line, which is connected to the large mobility of the electrons.[17,18] As the electron mass is increased, the mode is more localized and the self-interaction is assumed be weaker. This is investigated with simulations on the grid G2 with the standard parameter set and an increased electron-ion-mass-ratio of $m_e/m_i = 1.65 \times 10^{-2}$ and $m_e/m_i = 1.0$. In these simulations, a reduction in the intensity of the spikes is indeed observed. This is exemplarily shown for $m_e/m_i = 1.65 \times 10^{-2}$ in Fig. 7, where a clear reduction compared to the standard G2 case is visible, which proves the assumption.

The wave vectors of the driven zonal modes also depend on the value of the magnetic shear $\hat{s}$, as it is clear from Eq.

(6). If the magnetic shear is varied, the wave vectors of the driven zonal flows should vary correspondingly. To test this impact, simulations for magnetic shear values $\hat{s} \in \{0.156, 0.312, 1.092, 1.404\}$ have been performed with a grid resolution G2. The parameter $i_{k\psi}$ has to be adapted accordingly, using $i_{k\psi} \in \{1, 2, 7, 9\}$ for the respective shear cases. As an example, the radial spectrum of the electrostatic potential of a simulation with $\hat{s} = 1.092$ is shown in Fig. 8. In this and all other simulations, the expected spike position, calculated following Eq. (6), is found to be in perfect agreement with the position of the spikes in the k_ψ spectrum of the zonal flows. Because $i_{k\psi}$ has to decrease for smaller values, the overall drive through self-interaction increases, in turn decreasing the relative spike size (not shown). However, the influence on the radial shear profile remains and strong small scale structures dominate. The simulations with a higher $\hat{s}$ show a smaller influence of self-interaction, which can be seen in Fig. 8. This especially concerns $\omega_{E \times B}$ at higher k_ψ. Comparing $\omega_{E \times B}$ of the simulation with $\hat{s} = 1.092$ to a corresponding simulation with $\hat{s} = 0.78$, a reduction is visible. It is attributed to the lower density of modes that are affected by the self-interaction.

VI. STAIRCASE STRUCTURES WITH KINETIC ELECTRONS

The dependence on the magnetic shear allows the investigation of pattern formation in the $E \times B$ shear avoiding, to some extent, the small scale structures. Exemplarily, a scan over R/L_T at $\hat{s} = 1.092$ is carried out. This leads to a reappearance of the staircase structure and most of the typical traits associated with it.[4]

As an example, the evolution of the radial $E \times B$ shear rate of a simulation at $R/L_T = 3.6$ is depicted in Fig. 9 together with the evolution of the averaged heat conduction coefficient χ. A clear correspondence between periods with a marked decrease in the small scale structures and a suppressed heat flux is visible. Eventually, an established stationary state with a suppressed heat flux is reached. Here, a
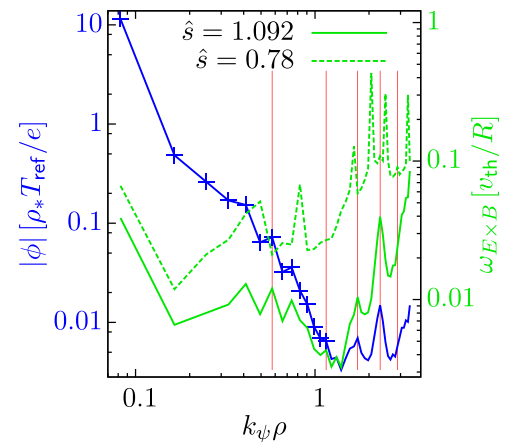

FIG. 8. Radial spectrum of the zonal potential (left axis and blue in the online version) and $E \times B$ shear (right axis and green in the online version), averaged over a stationary state with suppressed turbulence. The simulations uses the grid G2 and the standard parameter set but with an increased magnetic shear of $\hat{s} = 1.092$. As a comparison, the $E \times B$ shear of a simulation with the standard parameter set is depicted.
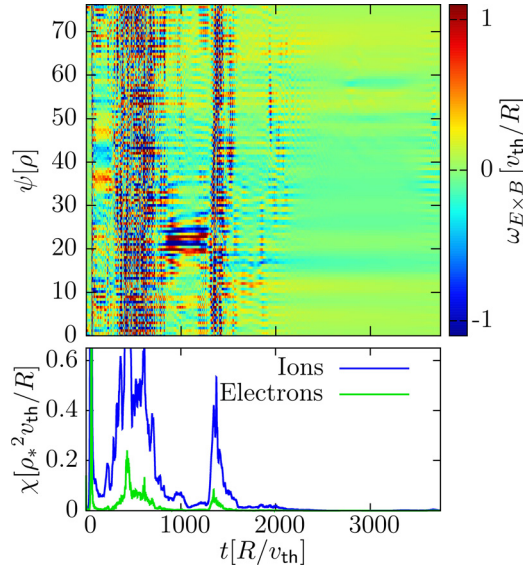
FIG. 9. Top: Time evolution of the radial $E \times B$ shear profile $\omega_{E \times B}$ of a simulation where the mechanism is weakened due to a different magnetic shear. It uses the grid size G2 and the standard parameters except $\hat{s} = 1.092$ and $R/L_T = 3.6$. The colour range of $\omega_{E \times B}$ is clipped to improve visibility. Bottom: Corresponding time evolution of the flux surface averaged heat conductivity χ.

staircase structure in the $E \times B$ shear can be identified, as shown in Fig. 10. Correspondingly, the spikes in the radial spectrum are weak. Compared to adiabatic simulations, a higher shear is found in the suppressed state which is attributed to the albeit small but still present small scale fluctuations.

Furthermore, a coincidence between this large scale structure and a radial localization of heat flux avalanches similar to the observations in adiabatic simulations[2–4] can be made out. To show this, the radial profile of the heat
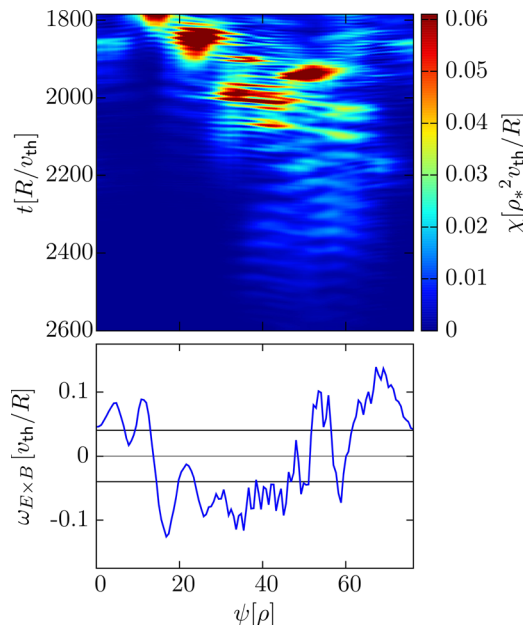

FIG. 10. Top: Radial heat conductivity profile of a simulation with $\hat{s} = 1.092$ and $R/L_T = 3.6$ on a grid G2. Bottom: Corresponding radial $E \times B$ shear profile averaged over a stationary period. Mind the periodic boundary conditions.

conductivity in the period where a staircase structure appears is shown in Fig. 10. Here, avalanches can be observed; however, they are considerably weaker compared to adiabatic simulations, as described in Ref. 22. Nevertheless, a relation between the avalanche source- and sink-regions and the staircase is visible (mind the periodic boundary conditions): They emerge from the flank of the staircase at $\psi \approx 15\rho$ and run towards a region at $\psi \approx 50\rho - 60\rho$. In accordance with the flattened flank, no exact sink-region can be identified. It should also be noted that the (local) strength of the avalanches coincides with local small scale perturbations of the staircase structure caused by self-interaction, visible, for example, around $t \approx 2000v_{\text{th}}/R$.

Also, the heat conductivity in the stationary state for varying R/L_T is examined; the results are shown in Fig. 2. A shift in the threshold compared to the simulations at $\hat{s} = 0.78$ is visible. This is associated with the increased magnetic shear, leading to a weakening of the ITG instability. The typical abrupt drop in the heat flux cannot be made out. It should be noted that the simulations close to the threshold do exhibit short states with suppressed turbulence; however no final, i.e., long term, stationary state is observed despite long simulation times. If the curve for an increased $\hat{s}$ is compared to the results from standard parameters, a difference for small heat conductivities $\chi \lesssim 1$ is visible. Where for standard parameters a small but finite χ is found, for an increased $\hat{s}$ the heat conductivity does go approximately linear to zero. This difference can be attributed to the appearance of the staircase structure and is backed by considerably long simulations.

It is concluded that staircase structures do form in simulations with kinetic electrons. The fact that the various signatures are only observed when reducing the self-interaction gives strong support to the idea that the small scale $E \times B$ shearing rate structures prevent the formation of staircases. Why the observed small scale structures do not suppress turbulence as efficiently as large scale structures cannot be answered in the scope of this analysis; however, it will be a topic of future work.

VII. CONCLUSION

In this paper, staircase structures are shown to develop in gyro-kinetic simulations with kinetic electrons. Staircases, however, do not develop under all circumstances. In many cases, a large amplitude small scale structure in the $E \times B$ shearing rate is observed, and in these cases, no staircase structure can be identified. The heat flux then goes smoothly to zero when reducing the temperature gradient length, and no radial localization of avalanches is observed. The small scale $E \times B$ shearing rate structures are interpreted to disrupt the formation of the larger scale staircase structures. This interpretation is empirically obtained since there is at present no convincing explanation for the staircase formation.

The small scale structures observed in the $E \times B$ shearing rate are interpreted as being driven by the self-interaction of turbulent modes that is generated over the periodic boundary conditions of the double periodic torus. While the ITG mode with adiabatic electrons is localized along the

magnetic field and shows no appreciable self-interaction, the mechanism is present in the case of kinetic electrons due to the extended mode structure. A proper numerical evaluation of the effect can only be obtained when the whole flux surface is treated, and consequently, a flux tube simulation that covers only part of the toroidal circumference can produce spurious results near the nonlinear threshold of turbulence generation. It should be noted that global simulations in which a wedge rather than the full flux surface is treated suffer from the same deficiency. The self-interaction is shown to decrease with the number of toroidal modes kept in the simulation, and for a full flux surface simulation scales proportional to ρ_*. It is to be expected that the effect is small in a reactor plasma, but at $\rho_* = 5 \times 10^{-3}$ it is still dominantly present and it is therefore likely that it is of importance to present day experiments. Also the magnetic shear is observed to affect the results through their impact on the boundary conditions. This dependence was utilized to generate conditions under which staircases can be observed to form.

ACKNOWLEDGMENTS

[1]G. Dif-Pradalier, P. H. Diamond, V. Grandgirard, Y. Sarazin, J. Abiteboul, X. Garbet, P. Ghendrih, A. Strugarek, S. Ku, and C. S. Chang, Phys. Rev. E **82**, 025401 (2010).

[2]G. Dif-Pradalier, G. Hornung, P. Ghendrih, Y. Sarazin, F. Clairet, L. Vermare, P. H. Diamond, J. Abiteboul, T. Cartier-Michaud, C. Ehrlacher, D. Estève, X. Garbet, V. Grandgirard, O. D. Gürcan, P. Hennequin, Y. Kosuga, G. Latu, P. Maget, P. Morel, C. Norscini, R. Sabot, and A. Storelli, Phys. Rev. Lett. **114**, 085004 (2015).

[3]F. Rath, A. G. Peeters, R. Buchholz, S. R. Grosshauser, P. Migliano, A. Weikl, and D. Strintzi, Phys. Plasmas **23**, 052309 (2016).

[4]A. G. Peeters, F. Rath, R. Buchholz, Y. Camenen, J. Candy, F. J. Casson, S. R. Grosshauser, W. A. Hornsby, D. Strintzi, and A. Weikl, Phys. Plasmas **23**, 082517 (2016).

[5]A. Weikl, A. G. Peeters, F. Rath, S. R. Grosshauser, R. Buchholz, W. A. Hornsby, F. Seiferling, and D. Strintzi, Phys. Plasmas **24**, 102317 (2017).

[6]G. Dif-Pradalier, G. Hornung, X. Garbet, P. Ghendrih, V. Grandgirard, G. Latu, and Y. Sarazin, Nucl. Fusion **57**, 066026 (2017).

[7]J. W. Connor, R. J. Hastie, and J. B. Taylor, Phys. Rev. Lett. **40**, 396 (1978).

[8]M. A. Beer, S. C. Cowley, and G. W. Hammett, Phys. Plasmas **2**, 2687 (1995).

[9]A. Peeters, Y. Camenen, F. Casson, W. Hornsby, A. Snodin, D. Strintzi, and G. Szepesi, "40 YEARS OF CPC: A celebratory issue focused on quality software for high performance, grid and novel computing architectures," Comput. Phys. Commun. **180**, 2650 (2009).

[10]S. Hamada, Nucl. Fission Res. Jpn. **1**, 542 (1958).

[11]S. Hamada, Nucl. Fusion **2**, 23 (1962).

[12]B. Scott, Phys. Plasmas **5**, 2334 (1998).

[13]B. Scott, Phys. Plasmas **8**, 447 (2001).

[14]A. I. Smolyakov, P. H. Diamond, and V. I. Shevchenko, Phys. Plasmas **7**, 1349 (2000).

[15]L. Chen, Z. Lin, and R. White, Phys. Plasmas **7**, 3129 (2000).

[16]T.-H. Watanabe, H. Sugama, A. Ishizawa, and M. Nunami, Phys. Plasmas **22**, 022507 (2015).

[17]K. Hallatschek and W. Dorland, Phys. Rev. Lett. **95**, 055002 (2005).

[18]C. Angioni, R. Duxand, E. Fableand, A. Peeters, and the ASDEX Upgrade Team, Plasma Phys. Controlled Fusion **49**, 2027 (2007).

[19]F. L. Hinton and M. N. Rosenbluth, Plasma Phys. Controlled Fusion **41**, A653 (1999).

[20]R. E. Waltz, G. D. Kerbel, and J. Milovich, Phys. Plasmas **1**, 2229 (1994).

[21]T. S. Hahm, M. A. Beer, Z. Lin, G. W. Hammett, W. W. Lee, and W. M. Tang, Phys. Plasmas **6**, 922 (1999).

[22]T. Görler, X. Lapillonne, S. Brunner, T. Dannert, F. Jenko, S. K. Aghdam, P. Marcus, B. F. McMillan, F. Merz, O. Sauter, D. Told, and L. Villard, Phys. Plasmas **18**, 056103 (2011).